

Leveraging Inpainting for Single-Image Shadow Removal

Xiaoguang Li¹*, Qing Guo^{2*}†, Rabab Abdelfattah¹, Di Lin³,
Wei Feng³, Ivor Tsang², Song Wang¹

¹University of South Carolina, USA, ²Center for Frontier AI Research (CFAR), A*STAR, Singapore,
³Tianjin University, China

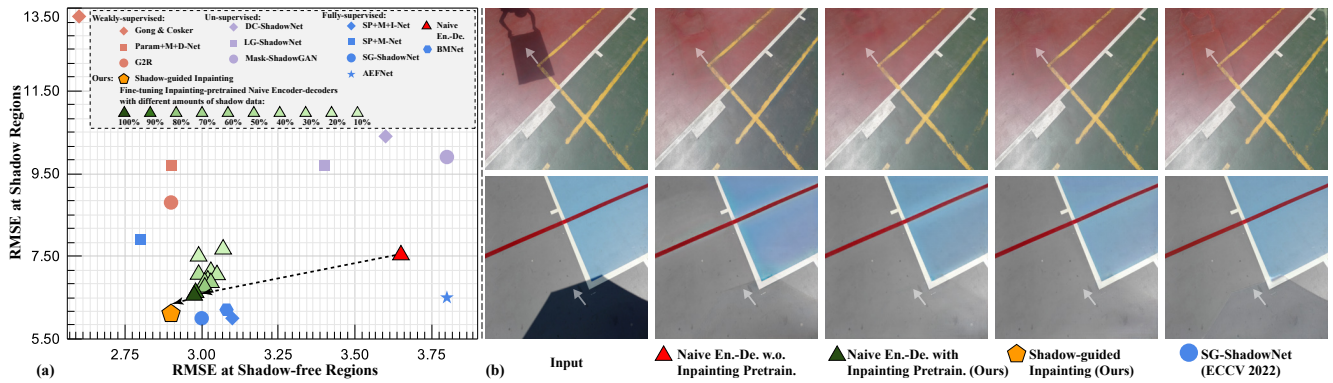


Figure 1. (a) Comparison with SOTA methods on ISTD+ dataset [21] at shadow (Y-axis) and shadow-free (X-axis) regions. We also present the results of a naive encoder-decoder network (Naive En.-De.) trained with different strategies: (1) training on inpainting data and fine-tuning on different amounts of shadow data; (2) only training on all shadow data. (b) displays two examples of four methods and we use white arrows to highlight the main advantages.

Abstract

Fully-supervised shadow removal methods achieve best restoration qualities on public datasets but still generate some shadow remnants. One of the reasons is the lack of large-scale shadow & shadow-free image pairs. Unsupervised methods can alleviate the issue but their restoration qualities are much lower than those of fully-supervised methods. In this work, we find that pretraining shadow removal networks on the image inpainting dataset can reduce the shadow remnants significantly: a naive encoder-decoder network gets competitive restoration quality w.r.t. the state-of-the-art methods via only 10% shadow & shadow-free image pairs. We further analyze the difference between networks with/without inpainting pretraining and observe that: inpainting pretraining enhances networks' capability of filling missing semantic information; shadow removal fine-tuning makes the networks know how to fill details of the shadow regions. Inspired by the above observations, we formulate shadow removal as a shadow-guided inpainting task to take advantage of the shadow removal and image inpainting. Specifically, we build a shadow-informed dynamic filtering network with two branches: the image

inpainting branch takes the shadow-masked image as input while the second branch takes the shadow image as input and is to estimate dynamic kernels and offsets for the first branch to provide missing semantic information and details. The extensive experiments show that our method empowered with inpainting outperforms all state-of-the-art methods. We release our code and models at <https://github.com/tsingqguo/inpaint4shadow>.

1. Introduction

Shadows in images are formed when some objects block the light source, which not only reduces the image quality but also affects the subsequent intelligent tasks like visual object detection [30], object tracking [33], face recognition [40], face landmark detection [7], etc. Single-image shadow removal is to map the shadow regions to their shadow-free counterparts, which can enhance the visual quality and benefit the intelligent tasks.

In recent years, with the development of advanced learning algorithms and deep architectures (i.e., GAN [10] and CycleGAN [42]), deep learning-based shadow removal methods [8, 22, 34] have achieved significant progress and ob-

tained top restoration qualities on public datasets. However, these methods may still lead to some shadow remnants. As the two cases shown in Fig. 1, even the state-of-the-art method SG-ShadowNet [34] generates obviously inconsistent colors across shadow boundaries. One of the reasons is the lack of large-scale shadow & shadow-free image pairs. The commonly-used ISTD+ dataset [21] only contains 1330 pairs of shadow and shadow-free images for training. To alleviate the requirements for the amounts of image pairs, researchers also develop weakly-supervised [9, 22, 27] and unsupervised shadow removal methods [18, 19, 26, 27]. However, all these methods still have a large gap to the fully-supervised methods (See the results in Fig. 1 (a)).

Meanwhile, several works [16, 36] have demonstrated that pretraining networks to predict masked patches from unmasked patches on a large-scale dataset can enhance the fully-supervised training on another small-scale dataset significantly. Actually, the task predicting masked patches is a special image inpainting task [24] that aims to fill missing pixels. Inspired by these works, we seek to leverage the image inpainting task for high-quality shadow removal. Specifically, given a deep network, we first train it on the image inpainting dataset where we can mask all clean images randomly and get large-scale clean & masked image pairs for free. Then, we finetune the network on the shadow removal dataset with limited shadow & shadow-free image pairs. As shown in Fig. 1, a naive encoder-decoder network pretrained on the inpainting dataset and fine-tuned on the 10% shadow data can achieve competitive restoration qualities (*i.e.* RMSE) at the shadow regions w.r.t. the state-of-the-art methods (*e.g.*, SP+M-Net [21]). Moreover, when we compare the networks with and without inpainting pretraining in the Fig. 1 (b), we see that inpainting pretraining can eliminate the shadow remnants effectively.

We further analyze the features of the networks with/without inpainting pretraining and see that inpainting pretraining enhances networks' capability of filling missed semantic information, and shadow removal finetuning makes the networks know how to fill details of the shadow regions. To utilize the respective advantages of the two tasks, we identify the shadow-guided inpainting task that regards the shadow removal as a special image inpainting task where we first crop the shadow regions and then try to fill the masked pixels under the guidance of the input shadow image. To address this task, we propose the *shadow-informed dynamic filtering* network that contains two branches: the first branch is for image inpainting and takes the shadow-masked image as input; the second branch takes the shadow image as input and is to estimate dynamic kernels and offsets for the first branch to provide missing semantic information and details. Our final method outperforms all state-of-the-art methods on the public datasets (See Fig. 1(a)) and reduces the shadow remnants significantly.

2. Related Work

2.1. General Shadow Removal Methods

To reconstruct the shadow-free image from its shadow counterpart, previous methods [6] [5] [15] [37] [35] [11] [28] focus more on exploiting the priors information. [15] utilize illumination difference to distinguish the shadow and shadow-free regions, then recover the shadow-free image by a lighting model. [6] [5] rebuild the shadow-free image based on the gradient information. [11] proposes to learn a patch mapping function to perform shadow removal.

Recently, deep learning-based methods have achieved excellent performance in shadow removal. [21] decomposes the shadow image as its shadow-free counterpart and a set of shadow parameters and uses illumination transformation to remove the shadow. [43] claims that the networks of shadow removal and generation can mutually promote, then propose a unified framework to perform shadow removal and generation together. [2] [34] design a feature transformation network to transform the contextual information from non-shadow regions to shadow regions. [8] reformulate the shadow removal as an exposure fusion problem, utilizing the deep neuron network to predict the parameters of exposure. Although achieving a remarkable result, the above supervised-based methods require a large amount of paired shadow & shadow-free images to train the network. To alleviate this limitation, the unsupervised methods [19] [26] [18] [27] employ the generative adversarial network (GAN) to train the network with large numbers of unpaired shadow & shadow-free images. However, the restoration results of unsupervised methods are not satisfied. In this work, we reformulate shadow removal as a shadow-guided inpainting task and propose a novel shadow-informed dynamic filtering network for shadow removal.

2.2. Predictive Filtering-based Image Restorations

The predictive filtering technique has been widely used for image processing [1] [29] [3] [12] [38]. Different from the traditional convolutional neural network (CNN) which shares the same kernel along the spacial level for each convolution layer, the predictive filtering technique predicts unique kernel for each location by using a deep neural network which makes it can utilize the neighbors' information explicitly. [14] use the predictive filtering on image level for deraining. [13] employ it to improve the performance of the generative adversarial network (GAN) based inpainting methods. [24] extend the image level filtering into the feature level and design an end-to-end image inpainting pipeline that can restore the images with large missing regions. Inspired by [24], in this work, we exploit predictive filtering to transfer the information from the non-shadow regions to the shadow regions to perform shadow removal.

3. Leveraging Inpainting-pretrained Networks for Shadow Removal

In this section, we first train a naive encoder-decoder network through an inpainting dataset (See Sec. 3.1). Then, we train the same network with paired shadow & shadow-free images (See Sec. 3.2) based on the inpainting-pretrained network and randomly initialized network, respectively. We conduct extensive empirical study and analysis in Sec. 3.3.

3.1. Training Network for Image Inpainting

Given a corrupted image I where some regions are cropped and indicated by a mask M , an image inpainting network is to fill the missing pixels and generate an image that is desired to be identical to the ground truth image (*i.e.*, I^*). To train the network, we obtain the corrupted image I by cropping the ground truth image I^* according to the mask, and then the image pair (I, I^*) forms a training example.

Here, we use the following setups for training an image inpainting network: **1** Network architecture. Instead of using advanced inpainting networks (*e.g.*, MISF [24]), we employ a naive encoder-decoder network that contains 11 convolution layers for the encoder and 3 transpose convolution layers for the decoder. Please check the architecture details in the supplementary material. By doing this, we can avoid the effects of some advanced designs on the observations. **2** Dataset and masks. We train the encoder-decoder network on the *Places2* dataset [41] that is widely used in the inpainting field. We randomly sample masks from a third-party mask dataset [25] and use them to crop the clean images. **3** Loss functions. We follow the designs of [24] and use the GAN loss, perceptual loss, and L_1 loss for training (See details in the supplementary material). With the above setups, we can train a naive encoder-decoder network for image inpainting.

3.2. Training Network for Shadow Removal

Given a shadow image I and a shadow mask M , a shadow removal network is to map the shadow regions indicated by the mask to their shadow-free counterparts and is desired to produce a clean image I^* . In contrast to the image inpainting task, we can hardly collect numerous paired images (*i.e.*, (I, I^*)) for training the shadow removal network since the corrupted image cannot be naively simulated via the ground truth image I^* and the two images should be captured under the same scene and the same environmental factors. Even the widely-used ISTD+ dataset [21] only contains 1,330 pairs of shadow and shadow-free images for training.

Here, we use the following setups for training a shadow removal network: **1** Network architecture. We employ the same encoder-decoder network in Sec. 3.1. **2** Dataset and masks. We use the ISTD+ dataset [21] for network training and testing where the shadow mask for each image is

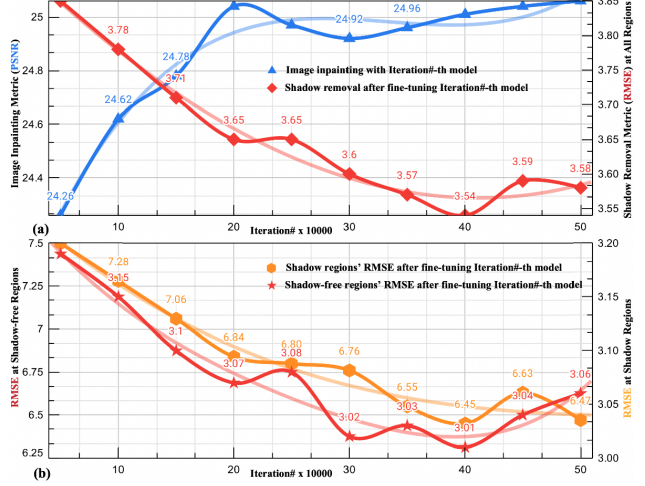


Figure 2. We first train the naive encoder-decoder network on the Places2 dataset and save the networks every 5×10^5 iterations, and then fine-tune each model with the shadow removal dataset (*i.e.*, ISTD+ [21]). The blue line in (a) presents the inpainting results (*i.e.*, PSNR) of different networks on the Places2 dataset, and the red line shows shadow removal results (*i.e.*, root mean square error (RMSE)) of fine-tuned networks on both shadow and shadow-free regions. (b) presents the shadow removal results (*i.e.*, RMSE) on the shadow regions and shadow-free regions, respectively.

given. **3** Loss functions. We only use L_1 loss for training (See details in the supplementary material). Then, we set up two training strategies: *First*, we randomly initialize the network's weights and train the network following the inpainting task but with the ISTD+ dataset [21]. *Second*, we use the inpainting-pretrained network as the initialization and fine-tuning the network via the ISTD+ dataset [21]. Based on the above setups, we can study how inpainting affects the shadow removal network training.

3.3. Empirical Study and Analysis

Fine-tuning inpainting-pretrained networks for shadow removal. Following the setups in Sec. 3.1, we first train an encoder-decoder network for image inpainting and store the intermediate models every 5×10^5 iterations. Then, we fine-tune these intermediate models on the shadow removal dataset (See Sec. 3.2). We show the inpainting results (*i.e.*, PSNR) of the intermediate models and the corresponding shadow removal performance (*i.e.*, RMSE) after fine-tuning in Fig. 1(a) and Fig. 2. We see that: **1** All shadow removal networks (*i.e.*, green triangles in Fig. 1(a)) that are fine-tuned on the inpainting-pretrained models achieve much lower RMSEs at both shadow and shadow-free regions than the network trained on the randomly initialized model (*i.e.*, red triangle in Fig. 1(a)). This demonstrates that inpainting pretraining indeed helps shadow removal task get much higher restoration quality in both shadow and shadow-free regions. **2** As the iteration becomes larger, the inpainting capability of intermediate models increases (*i.e.*, the PSNR on the inpainting dataset

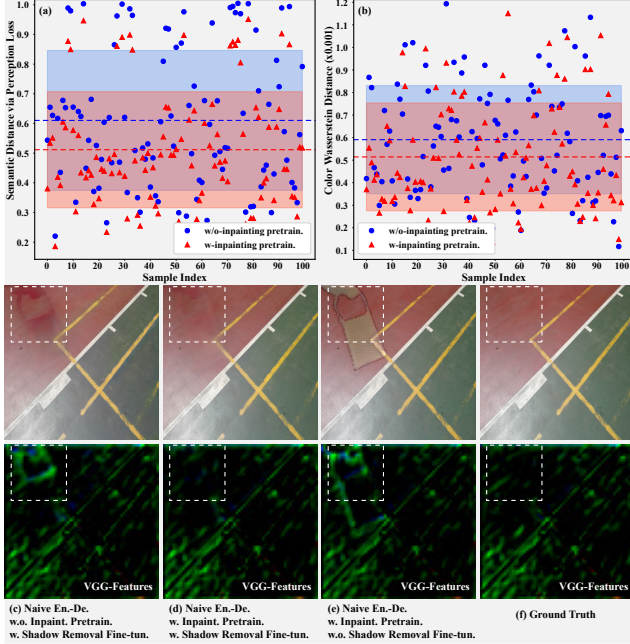


Figure 3. (a) shows the semantic distance (*i.e.*, VGG-feature-based perception loss) between the shadow-removed image and its ground truth. (b) presents the color distance (*i.e.*, Wasserstein distance) between the shadow-removed color histogram and its ground truth histogram. The dashed lines and colorful rectangles denote the mean values and standard deviation across all examples. Other subfigures (c), (d), (e), and (f) compare the VGG features of shadow-removed images and their ground truth images.

increases) and the corresponding fine-tuned shadow removal networks get lower RMSEs at the shadow and shadow-free regions. This observation demonstrates that the shadow removal performance is related to the inpainting capability of pretrained models, directly.

Fine-tuning inpainting-pretrained networks with different amounts of shadow & shadow-free image pairs. With an adequately inpainting-pretrained network, we use different amounts of shadow & shadow-free image pairs that are randomly selected from the ISTD+ [21] to fine-tune the network, respectively. As shown in Fig. 1 (a), we see that: ❶ With only 10% ISTD+ [21], the fine-tuned encoder-decoder network achieves lower RMSE at shadow-free regions than the state-of-the-art method AEFNet [8] (*i.e.*, 3.07 vs. 3.80) and lower RMSE on shadow regions than the SP+M-Net method (*i.e.*, 7.67 vs. 7.9). Both methods are trained with all examples in ISTD+ dataset [21]. ❷ Inpainting-pretrained networks are fine-tuned with different amounts of image pairs and have similar RMSEs at both shadow and shadow-free regions. ❸ The network fine-tuned with 100% image pairs outperforms three recent works including SG-ShadowNet [34], SP+M+I-Net [23], and AEFNet [8] at the shadow-free regions, which demonstrates that inpainting pretraining benefits the shadow-free preservation.

Feature analysis with/without inpainting pretraining. To further understand the advantages of inpainting pretrain-

ing for shadow removal, we use the naive encoder-decoder network with/without inpainting pretraining to handle 100 images randomly selected from the ISTD+ dataset [21]. Then, we calculate the VGG-feature-based perception loss [20] as the semantic distance between each restored image and its ground truth image (*i.e.*, one point in Fig. 3 (a)). We also count the color histograms of each restored image and its ground truth and calculate the Wasserstein distance between the two histograms (*i.e.*, one point in Fig. 3 (b)). We see that: ❶ The restored images of the inpainting-pretrained network have much lower semantic distance w.r.t. the ground truth than those of the network without inpainting pretraining, which demonstrates that inpainting pretraining can enhance the network’s capability of recovering degraded semantic information, significantly. ❷ The recovered semantic information further benefits the elimination of the color distance (See Fig. 3 (b)). Comparing Fig. 3 (c) with (d), we see that the inpainting pretrained network can suppress the shadow patterns (*i.e.*, the white dashed rectangles) at both the semantic level and image level effectively.

Results with/without shadow-removal finetuning. We compare the inpainting pretrained network with/without shadow removal fine-tuning (See Fig. 3 (d) and (e)). Without the shadow removal fine-tuning, the network cannot recover the colors properly and the shadow patterns become more obvious. We have similar observations at the feature level.

4. Methodology

The above studies are based on the same network architecture and illustrate the functionalities of different kinds of training data. To further enhance the restoration quality, beyond the data-driven solution, we propose to reformulate the shadow removal as a special inpainting task, *i.e.*, shadow-guided inpainting, as detailed in Sec. 4.1, that aims to combine the advantages of the two tasks. To this end, we propose a new network, *i.e.*, *shadow-informed dynamic filtering* in Sec. 4.2, to realize the task in a unified architecture and detail the implementations in Sec. 4.3.

4.1. Shadow-guided Inpainting

Given a shadow image I and a binary mask M , we first crop the shadow regions and produce a shadow-masked image $\tilde{I} = I \odot (1 - M)$. Then, we aim to complete the cropped regions in \tilde{I} under the guidance of the shadow image I . We denote the whole process as the *shadow-guided inpainting* task. Intuitively, such a task inherits the advantages of image inpainting and could fill the missing semantic information with similar color distributions as the shadow-free regions (See discussions in Sec. 3.3). Besides, the task could recover missing details in the shadow regions since the whole information is contained in the raw shadow image. However, the implementation of this task is not straightforward.

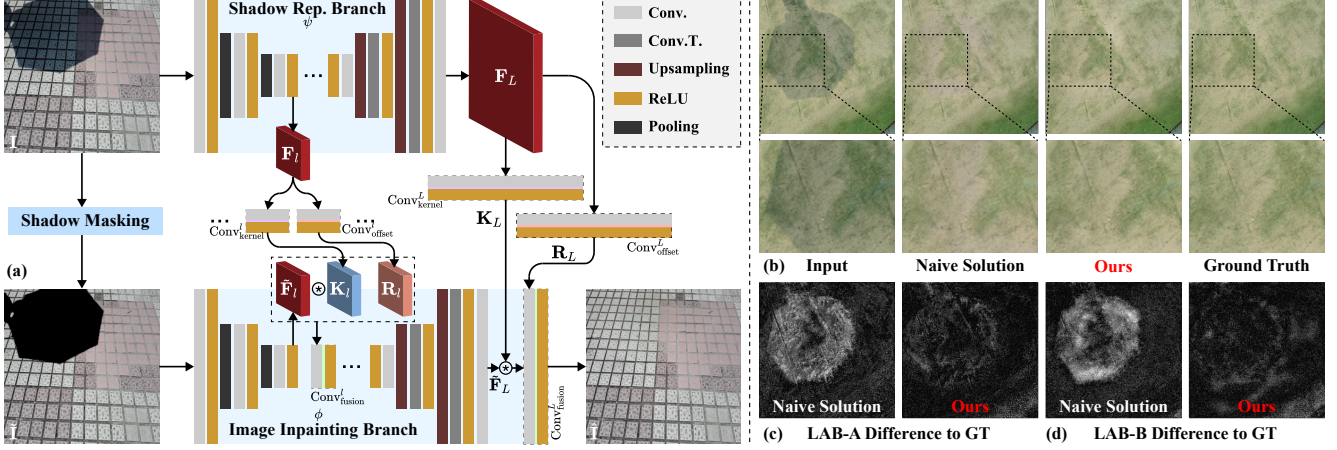


Figure 4. (a) displays the whole framework of the proposed shadow-informed dynamic filtering. (b) shows examples of using a simple shadow-guided inpainting solution and the proposed shadow-informed dynamic filtering to handle the shadow image, respectively. We also display the enlarged regions in the second row. We further calculate the color difference to the ground truth of the A channel (*i.e.*, (c)) and B channel (*i.e.*, (d)) in the LAB color space.

A simple solution is to concatenate the shadow-masked image and shadow image and feed them to the same encoder-decoder network used in the Sec. 3.1. We can also perform inpainting pretraining and shadow removal fine-tuning to that network. We show an example in Fig. 4 (b), (c), and (d). Clearly, the result of the naive solution still has an obvious color shifting to the ground truth (See the LAB-A/B differences in Fig. 4 (c) and (d)), which demonstrates that such a naive solution cannot properly take the advantages of both tasks and the color inconsistency still remains.

4.2. Shadow-informed Dynamic Filtering

Instead of concatenating the two images, we propose to handle the shadow image and shadow-masked image via two network branches, *i.e.*, the shadow representation branch and image inpainting branch, respectively and use the former branch to guide the image inpainting branch dynamically. We show the whole framework in Fig. 4(a).

The image inpainting branch is a dynamic encoder-decoder network and we denote it as $\phi(\cdot)$. It takes the shadow-masked image as input and we can represent the l th-layer feature $\tilde{\mathbf{F}}_l \in \mathbb{R}^{H_l \times W_l \times C_l}$ as

$$\tilde{\mathbf{F}}_l = \phi_l(\dots(\phi_2(\phi_1(\tilde{\mathbf{I}}, \mathbf{M}))), \quad (1)$$

where $\phi_l(\cdot)$ is the l th layer in the branch. Meanwhile, we can use the shadow representation branch (*i.e.*, $\psi(\cdot)$) to get the l th feature of the shadow image

$$\mathbf{F}_l = \psi_l(\dots(\psi_2(\psi_1(\mathbf{I}, \mathbf{M}))). \quad (2)$$

Instead of passing the shadow-masked feature (*i.e.*, $\tilde{\mathbf{F}}_l$) to subsequent layers of ϕ directly, we propose to process the feature via an element-wise kernel (*i.e.*, $\mathbf{K}_l \in \mathbb{R}^{H_l \times W_l \times K_l}$) and an offset $\mathbf{R}_l \in \mathbb{R}^{H_l \times W_l \times C_l}$, which are predicted from the shadow feature. We represent the whole process as

$$\tilde{\mathbf{F}}'_l = \text{Conv}_{\text{fusion}}^l(\tilde{\mathbf{F}}_l \otimes \mathbf{K}_l, \mathbf{R}_l), \quad (3)$$

where ‘ $\text{Conv}_{\text{fusion}}^l$ ’ denotes a convolution layer followed by a ReLU to fuse the offset and filtering-reconstructed feature. The operation ‘ \otimes ’ is the element-wise filtering [24] and the p th element reconstruction can be represented as

$$(\tilde{\mathbf{F}}_l \otimes \mathbf{K}_l)[p] = \sum_{\mathbf{q} \in \mathcal{N}_p} \mathbf{K}_l^p[\mathbf{q} - p] \tilde{\mathbf{F}}_l[\mathbf{q}], \quad (4)$$

where $\mathbf{K}_l^p \in \mathbb{R}^{K_l \times K_l}$ is reshaped from the p th element of \mathbf{K}_l and is the kernel for filtering the p th element of $\tilde{\mathbf{F}}_l$ via its K_l^2 neighboring elements, *i.e.*, \mathcal{N}_p . Intuitively, the element-wise filtering is to reconstruct each feature element via its neighboring elements while the offset tensor is to fill the missing elements in the shadow regions. The key problem is how to estimate the kernel and offset tensors adaptively and dynamically w.r.t. different shadows and inputs. Here, we use the shadow features in Eq. (2) to achieve the goal

$$\mathbf{K}_l = \text{Conv}_{\text{kernel}}^l(\mathbf{F}_l), \mathbf{R}_l = \text{Conv}_{\text{offset}}^l(\mathbf{F}_l), \quad (5)$$

where $\text{Conv}_{\text{kernel}}(\cdot)$ and $\text{Conv}_{\text{offset}}(\cdot)$ are two convolutional layers that transfer the shadow feature to the element-wise kernel and offset, respectively. We validate the functionalities of the kernel and offset in the experimental section. The reconstructed feature $\tilde{\mathbf{F}}'_l$ is further fed to the subsequent layers in ϕ to estimate a shadow-free image, *i.e.*, $\tilde{\mathbf{F}}'_L = \phi(\tilde{\mathbf{I}}, \mathbf{M})$.

Besides the feature-level shadow-guided filtering, we add the same architecture at the image level for detail refinement. Specifically, we feed the reconstructed l th feature to subsequent layers of the shadow representation branch $\psi(\cdot)$ and output the final feature $\mathbf{F}_L = \psi(\tilde{\mathbf{I}}, \mathbf{M})$ having the same resolution with the input image. Then, we also use two convolution layers to predict image-level kernel and offset (*i.e.*, $\mathbf{K}_L \in \mathbb{R}^{H \times W \times K^2}$ and $\mathbf{R}_L \in \mathbb{R}^{H \times W \times 3}$), respectively (See Fig. 4(a)). Then, we use the image-level kernel and

offset to handle the initially restored image $\tilde{\mathbf{F}}_L$ via a filtering operation and a convolution layer for fusion (See Eq. (3)). We get the final predicted image $\hat{\mathbf{I}}$.

4.3. Implementation Details

Network architectures. We set the image inpainting branch and the shadow representation branch as the same encoder-decoder network. The encoder consists of three convolution layers and each convolution layer is followed by a ReLU activation. The extracted feature by the encoder goes through eight Resnet blocks. The decoder also contains three transposition convolutions followed by a ReLU. Theoretically, we can add the dynamic filtering operation to all layers, which would lead to high complexity. Here, we equip the shadow-informed dynamic filtering to the third-layer features of ϕ and ψ and the predicted image. We employ the kernel of size three when performing the filtering on both image & feature levels. The $\text{Conv}_{\text{kernel}}^l$ and $\text{Conv}_{\text{offset}}^l$ contain a single-layer convolution with kernel size as 1 and a ReLU layer. In terms of the fusion layer, we use a convolution layer with a kernel of size three. We list all details of architecture in the supplementary material.

Loss functions. When training on the inpainting dataset, we follow [24] and use GAN loss, perceptual loss, Style loss, and L_1 loss, which guides the network to fill in missing semantic information and details. When fine-tuning the network on the shadow dataset, we only use L_1 loss to optimize since this stage mainly focuses on restoration fidelity. We introduce all loss functions in the supplementary material.

Training details. We first pretrain the network 450,000 iterations with batch size 8 on the Places2 dataset, then fine-tune it with 250,000 iterations under the same batch size on the shadow removal datasets. Following [8], the input images are resized to 256x256. We use Adam as the optimizer to optimize the network with a learning rate of 0.0001 and all the experiments are conducted on the Linux server with two NVIDIA Tesla V100 GPUs.

5. Experiments

5.1. Setups

Datasets. We first train our network on the image inpainting dataset (*i.e.*, Places2 challenge dataset [41]) and then fine-tune it on the ISTD+ [21] and SRD [32] datasets, respectively. Finally, we evaluate the trained networks on the ISTD+ [21] and SRD datasets [32]. The Places2 dataset contains more than millions of images under over 365 scenes. We use the irregular masks in [25]. The ISTD+ dataset [21] is constituted of 1330 triplets for training and 540 triplets for testing. We follow the previous method and use ground truth masks during the training. For the evaluation, we follow [8] using Ostu’s algorithm to calculate the difference between the shadow and shadow-free images to get the masks.

The SRD dataset [32] contains 2680 paired shadow and shadow-free images for training and 408 paired shadow and shadow-free images for testing without providing ground truth masks. Therefore, during the training and testing, we use the detected masks provided by DHAN [4].

Metrics. To prove the effectiveness of our method, we follow the previous method [8] to calculate the root mean square error (RMSE) between the reconstructed shadow-free images and the corresponding ground truth in the LAB color space. Besides, we also use the peak signal-to-noise ratio (PSNR [20]), structural similarity index (SSIM), and the learned perceptual image patch similarity (LPIPS [39]) to measure the quality of recovered shadow-free images.

Baselines. We compare our proposed method with ten state-of-the-art shadow removal methods which includes SP+M-Net [21], DSC [17], DHAN [4], Param+M+D-Net [22], LG-shadowNet [26], DC-ShadowNet [19], G2R-ShadowNet [27], Fu et al. [8], BMNet [43], and SG-ShadowNet [34].

5.2. Comparison Results

Quantitative comparison. We first compare our method with SP+M-Net [21], Param+M+D-Net [22], Fu et al. [8], LG-shadowNet [26], DC-ShadowNet [19], G2R-ShadowNet [27], BMNet [43], and SG-ShadowNet [34] on the ISTD+ dataset [21]. As shown in Table 1, we can observe that: ❶ for the shadow region, our method achieves a competitive result compared with SG-ShadowNet [34] over RMSE and BMNet [43] over SSIM. Besides, our method outperforms other competitors over all the metrics. When compared based on PSNR, our method can outperform all the competitors by a large margin. Specifically, compared with LG-shadowNet [26] and Fu et al. [8], our method can increase PSNR 15.80% and 3.84% respectively. ❷ for the non-shadow region, our method outperforms all the competitors over all metrics. Specifically, compared with LG-shadowNet [26] our method decreases RMSE 13.73%, increases PSNR 11.54%, and increases SSIM 0.89%. ❸ for the whole image, our method outperforms all the competitors including SG-ShadowNet [34] and BMNet [43] over each metric *i.e.* RMSE, PSNR, SSIM, and LPIPS. Specifically, our method decreases RMSE 4.45% and LPIPS 2.82% as well as increases PSNR 4.45% and SSIM 0.49% compared with BMNet [43]. When compared with SG-ShadowNet [34] our method decreases RMSE 2.71% and LPIPS 7.23% as well as increases PSNR 4.10% and SSIM 0.77% respectively.

Besides, we further compare with DSC [17], DHAN [4], Fu et al. [8], DC-ShadowNet [19], BMNet [43], and SG-ShadowNet [34] on the SRD dataset [32]. As shown in Table 2, we see that: for the shadow region, non-shadow region, and the whole image, our method outperforms all baselines over the four metrics, *i.e.*, RMSE, PSNR, SSIM, and LPIPS. Compared with DC-ShadowNet [19], in the

Table 1. Comparison results on ISTD+ dataset [21].

Method	All				Shadow			Non-Shadow		
	RMSE↓	PSNR↑	SSIM↑	LPIPS↓	RMSE↓	PSNR↑	SSIM↑	RMSE↓	PSNR↑	SSIM↑
SP+M-Net [21]	3.610	32.33	0.9479	0.0716	7.205	36.16	0.9871	2.913	35.84	0.9723
Param+M+D-Net [22]	4.045	30.12	0.9420	0.0759	9.714	33.59	0.9850	2.935	34.33	0.9723
Fu et al. [8]	4.278	29.43	0.8404	0.1673	6.583	36.41	0.9769	3.827	31.01	0.8755
LG-ShadowNet [26]	4.402	29.20	0.9335	0.0920	9.709	32.65	0.9806	3.363	33.36	0.9683
DC-ShadowNet [19]	4.781	28.76	0.9219	0.1112	10.434	32.20	0.9758	3.674	33.21	0.9630
G2R-ShadowNet [27]	3.970	30.49	0.9330	0.0868	8.872	34.01	0.9770	3.010	34.62	0.9707
BMNet [43]	3.595	32.30	0.9551	0.0567	6.189	37.30	0.9899	3.087	35.06	0.9738
SG-ShadowNet [34]	3.531	32.41	0.9524	0.0594	6.019	37.41	0.9893	3.044	34.95	0.9725
Ours	3.435	33.74	0.9598	0.0551	6.159	37.81	0.9891	2.901	37.21	0.9770

Table 2. Comparison results on SRD dataset [32].

Method	All				Shadow			Non-Shadow		
	RMSE↓	PSNR↑	SSIM↑	LPIPS↓	RMSE↓	PSNR↑	SSIM↑	RMSE↓	PSNR↑	SSIM↑
DSC [17]	5.704	29.01	0.9044	0.1145	8.828	34.20	0.9702	4.509	31.85	0.9555
DHAN [4]	4.666	30.67	0.9278	0.0792	7.771	37.05	0.9818	3.486	32.98	0.9591
Fu et al. [8]	6.269	27.90	0.8430	0.1820	8.927	36.13	0.9742	5.259	29.43	0.8888
DC-ShadowNet [19]	4.893	30.75	0.9118	0.1084	8.103	36.68	0.9759	3.674	33.10	0.9540
BMNet [43]	4.240	31.88	0.9376	0.0817	6.982	37.41	0.9816	3.198	35.09	0.9676
SG-ShadowNet [34]	4.297	31.31	0.9273	0.0835	7.564	36.55	0.9807	3.056	34.23	0.9611
Ours	3.778	33.33	0.9413	0.0752	6.020	39.57	0.9855	2.926	35.76	0.9678

shadow region, our method decreases RMSE 25.70% as well as increases PSNR 7.87% and SSIM 0.98%. In the non-shadow region, our method decreases RMSE 20.35% as well as increases PSNR 8.03% and SSIM 1.44%. In the whole image, our method decreases RMSE 22.78% and LPIPS 30.62% as well as increases PSNR 8.39% and SSIM 3.23%.

Qualitative comparison. We visualize four samples from ISTD+ [21] and SRD datasets [32] in Fig. 5. We can observe that ❶ our method can generate more natural and realistic color in the shadow regions of the restored result. As shown in Case2 and Case4, the generated floor in the shadow regions by our method is almost identical to the ground truth. Compared with other methods *i.e.* BMNet [43] and DSC [17], we can find obvious color inconsistencies between the shadow regions and non-shadow regions in their generated result. ❷ Although without any post process, the generated result by our method is more smooth along the shadow boundary than other methods generated. As shown in Case1, the boundary in our restored result is almost unidentified by human eyes. However, we can observe the boundary clearly in the restored result by other methods. Also in Case3, our restored result is almost identical to the ground truth. But we can find a clear ghost along the shadow boundary in restored results by other methods.

5.3. Ablation Study

To prove the effectiveness of each part of our method, we conduct the following experiments for ablations: **Exp1**, we remove the image-level filtering, feature-level filtering, and offset **R**, respectively, and get three variants (See first three rows of Table 3). Then, we pretrain each variant on the image inpainting dataset and fine-tune that on the shadow dataset. **Exp2**, we remove both image&feature-level filtering but retain the offset. We also perform the pretraining and fine-

tuning like exp1. **Exp3**, we pretrain a naive encoder-decode network on the image inpainting dataset and fine-tune it on the shadow dataset like Exp1 and Exp2. Meanwhile, we train another naive encoder-decode directly on the shadow dataset. As shown in Table 3, we have the following observations: ❶ Exp1 and Exp2 have a very close performance in the non-shadow regions as well as similar SSIM and PSNR in the shadow region, here we focus on analyzing the effectiveness of each variant in the shadow regions over RMSE. Without the image level filtering, feature level filtering, and offset **R** RMSE increase by 3.45%, 2.32%, and 5.35% respectively. When removing both image&feature level filtering, RMSE increases by 12.48%. Therefore, Exp1 and Exp2 can prove the effectiveness of each part of our method. ❷ The pre-trained encoder-decode outperforms its counterpart which is not pretrained a lot over RMSE, PSNR, and SSIM. Specifically, in the shadow region, it decreases RMSE 14.14% as well as increases PSNR 2.08% and SSIM 0.09%, in the non-shadow region, it decreases RMSE 17.25% as well as increases PSNR 2.41% and SSIM 0.25%, and in the whole image, it decreases RMSE 16.34% as well as increase PSNR 2.56% and SSIM 0.46%. Therefore, Exp3 can prove the effectiveness of pretraining on the image inpainting dataset.

We have provided a visualized feature comparison between the restored results from the naive encoder-decode with inpainting pretraining and its counterpart which is not pretrained as shown in Fig. 3 (d) and (c). we can observe that with inpainting pretraining, the extracted feature by VGG from the restored image is more close to the corresponding ground truth.

5.4. Relationship to SOTA Image Inpainting

For the single-image inpainting task, the input is a corrupted image as shown in Fig. 6 (a) which can be got by

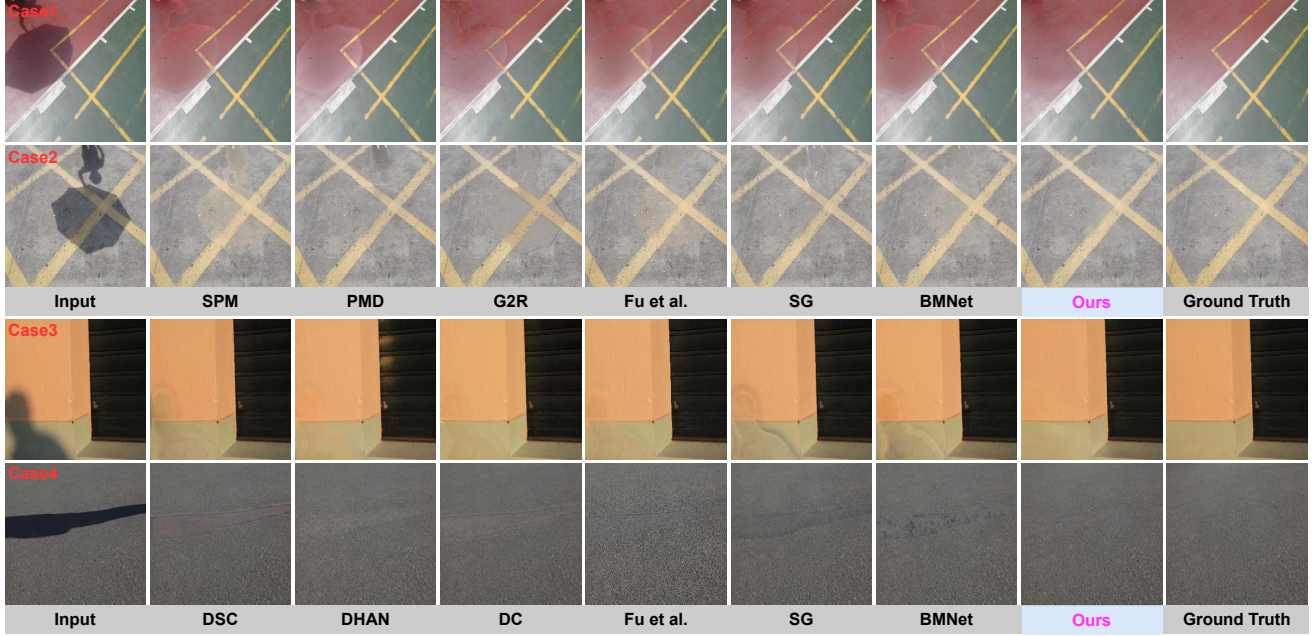


Figure 5. Visualization results on ISTD+ dataset [21] (first two rows) and SRD dataset [32] (last two rows)

Table 3. Ablition study on ISTD+ dataset [21].

Method	All				Shadow			Non-Shadow		
	RMSE↓	PSNR↑	SSIM↑	LPIPS↓	RMSE↓	PSNR↑	SSIM↑	RMSE↓	PSNR↑	SSIM↑
w/o image level filtering	3.468	33.66	0.9523	0.0552	6.372	37.74	0.9812	2.909	37.03	0.9694
w/o feature level filtering	3.468	33.66	0.9518	0.0567	6.302	37.80	0.9813	2.914	36.86	0.9687
w/o offset R	3.496	33.66	0.9511	0.0579	6.489	37.73	0.9808	2.910	36.94	0.9689
w/o image&feature level filtering	3.627	33.57	0.9573	0.0603	6.928	37.68	0.9884	2.981	36.87	0.9756
encoder-decode w pretraining	3.527	33.59	0.9589	0.0603	6.377	37.66	0.9886	2.969	36.96	0.9769
encoder-decode w/o pretraining	4.216	32.75	0.9545	0.0661	7.428	36.89	0.9877	3.588	36.09	0.9744
Ours	3.435	33.74	0.9598	0.0551	6.159	37.81	0.9891	2.901	37.21	0.9770

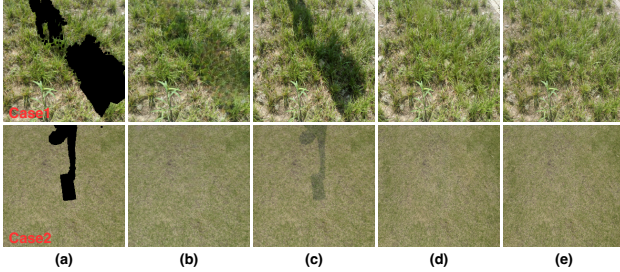


Figure 6. (a) and (b) are the input(cropped image) and restored result of [24]. (c) and (d) are the input(shadow image) and restored result of our method. (e) is the corresponding ground truth.

multiplying the original image with a binary mask. The masked regions are generated totally based on the unmasked background. For the shadow removal task, the input is a shadow image as shown in Fig. 6 (c) and the shadow regions is indicated by a binary mask. When the binary mask is small or thin *i.e.* (a) and (c) in Case2, the restored result of inpainting is indistinguishable compared with the restored result of shadow removal (see (b) and (d) in Case2). However, when the binary mask is large *i.e.* (a) and (c) in Case1, the texture information of the restored result based on inpainting is worse than the shadow removal-based counterpart. This is because the shadow regions *i.e.* (c) can provide more de-

tailed texture information than the masked regions *i.e.* (a). But from (b) in Case1, we can still find that the restored color in the masked regions is similar to the background. This phenomenon proves that the inpainting method has the capability to transfer the color from the background to the masked regions even when the masked regions is large. Based on the above observations, we can find the potential mutual promotion between image inpainting and shadow removal *i.e.* image inpainting and shadow removal can provide color and textual information respectively.

6. Conclusions

In this work, we found that pretraining a network on the image inpainting dataset and fine-tuning it on the paired shadow & shadow-free images can enhance the network’s capability for shadow removal significantly. We conducted extensive experiments to analyze and compare the networks with or without inpainting pretraining. Inspired by these studies, we reformulated shadow removal as a shadow-guided inpainting task and propose a novel shadow-informed dynamic filtering network for shadow removal. The extensive experiments show that our method empowered with inpainting outperforms all state-of-the-art methods.

Limitations. Our method is trained and evaluated on the widely used shadow datasets which cover a small portion of shadow scenarios in the real world. Hence, we may observe some fine-grained remnants around the shadow boundaries when the shadow patterns are complex. In future work, we will continue to address the weaknesses.

References

- [1] Steve Bako, Thijs Vogels, Brian McWilliams, Mark Meyer, Jan Novák, Alex Harvill, Pradeep Sen, Tony Derose, and Fabrice Rousselle. Kernel-predicting convolutional networks for denoising monte carlo renderings. *ACM Trans. Graph.*, 36(4):97–1, 2017.
- [2] Zipei Chen, Chengjiang Long, Ling Zhang, and Chunxia Xiao. Canet: A context-aware network for shadow removal. In *Proceedings of the IEEE/CVF International Conference on Computer Vision*, pages 4743–4752, 2021.
- [3] Yupeng Cheng, Felix Juefei-Xu, Qing Guo, Huazhu Fu, Xiaofei Xie, Shang-Wei Lin, Weisi Lin, and Yang Liu. Adversarial exposure attack on diabetic retinopathy imagery. *arXiv preprint arXiv:2009.09231*, 2020.
- [4] Xiaodong Cun, Chi-Man Pun, and Cheng Shi. Towards ghost-free shadow removal via dual hierarchical aggregation network and shadow matting gan. In *Proceedings of the AAAI Conference on Artificial Intelligence*, volume 34, pages 10680–10687, 2020.
- [5] Graham D Finlayson, Mark S Drew, and Cheng Lu. Entropy minimization for shadow removal. *International Journal of Computer Vision*, 85(1):35–57, 2009.
- [6] Graham D Finlayson, Steven D Hordley, Cheng Lu, and Mark S Drew. On the removal of shadows from images. *IEEE transactions on pattern analysis and machine intelligence*, 28(1):59–68, 2005.
- [7] Lan Fu, Qing Guo, Felix Juefei-Xu, Hongkai Yu, Wei Feng, Yang Liu, and Song Wang. Benchmarking shadow removal for facial landmark detection and beyond. *arXiv preprint arXiv:2111.13790*, 2021.
- [8] Lan Fu, Changqing Zhou, Qing Guo, Felix Juefei-Xu, Hongkai Yu, Wei Feng, Yang Liu, and Song Wang. Auto-exposure fusion for single-image shadow removal. In *Proceedings of the IEEE/CVF International Conference on Computer Vision*, pages 10571–10580, 2021.
- [9] Han Gong and Darren Cosker. Interactive removal and ground truth for difficult shadow scenes. *JOSA A*, 33(9):1798–1811, 2016.
- [10] Ian Goodfellow, Jean Pouget-Abadie, Mehdi Mirza, Bing Xu, David Warde-Farley, Sherjil Ozair, Aaron Courville, and Yoshua Bengio. Generative adversarial networks. *Communications of the ACM*, 63(11):139–144, 2020.
- [11] Maciej Gryka, Michael Terry, and Gabriel J Brostow. Learning to remove soft shadows. *ACM Transactions on Graphics (TOG)*, 34(5):1–15, 2015.
- [12] Qing Guo, Felix Juefei-Xu, Xiaofei Xie, Lei Ma, Jian Wang, Bing Yu, Wei Feng, and Yang Liu. Watch out! motion is blurring the vision of your deep neural networks. *Advances in Neural Information Processing Systems*, 33, 2020.
- [13] Qing Guo, Xiaoguang Li, Felix Juefei-Xu, Hongkai Yu, Yang Liu, and Song Wang. Jpgnet: Joint predictive filtering and generative network for image inpainting. In *Proceedings of the 29th ACM International Conference on Multimedia*, pages 386–394, 2021.
- [14] Qing Guo, Jingyang Sun, Felix Juefei-Xu, Lei Ma, Xiaofei Xie, Wei Feng, Yang Liu, and Jianjun Zhao. Efficientderain: Learning pixel-wise dilation filtering for high-efficiency single-image deraining. In *Proceedings of the AAAI Conference on Artificial Intelligence*, volume 35, pages 1487–1495, 2021.
- [15] Ruiqi Guo, Qieyun Dai, and Derek Hoiem. Paired regions for shadow detection and removal. *IEEE transactions on pattern analysis and machine intelligence*, 35(12):2956–2967, 2012.
- [16] Kaiming He, Xinlei Chen, Saining Xie, Yanghao Li, Piotr Dollár, and Ross Girshick. Masked autoencoders are scalable vision learners. In *Proceedings of the IEEE/CVF Conference on Computer Vision and Pattern Recognition*, pages 16000–16009, 2022.
- [17] Xiaowei Hu, Chi-Wing Fu, Lei Zhu, Jing Qin, and Pheng-Ann Heng. Direction-aware spatial context features for shadow detection and removal. *IEEE TPAMI*, 42(11):2795–2808, 2019.
- [18] Xiaowei Hu, Yitong Jiang, Chi-Wing Fu, and Pheng-Ann Heng. Mask-shadowgan: Learning to remove shadows from unpaired data. In *Proceedings of the IEEE/CVF International Conference on Computer Vision*, pages 2472–2481, 2019.
- [19] Yeying Jin, Aashish Sharma, and Robby T Tan. Dc-shadownet: Single-image hard and soft shadow removal using unsupervised domain-classifier guided network. In *Proceedings of the IEEE/CVF International Conference on Computer Vision*, pages 5027–5036, 2021.
- [20] Justin Johnson, Alexandre Alahi, and Li Fei-Fei. Perceptual losses for real-time style transfer and super-resolution. In *European conference on computer vision*, pages 694–711. Springer, 2016.
- [21] Hieu Le and Dimitris Samaras. Shadow removal via shadow image decomposition. In *Proceedings of the IEEE/CVF International Conference on Computer Vision*, pages 8578–8587, 2019.
- [22] Hieu Le and Dimitris Samaras. From shadow segmentation to shadow removal. In *European Conference on Computer Vision*, pages 264–281. Springer, 2020.
- [23] Hieu Le and Dimitris Samaras. Physics-based shadow image decomposition for shadow removal. *IEEE Transactions on Pattern Analysis & Machine Intelligence*, (01):1–1, 2021.
- [24] Xiaoguang Li, Qing Guo, Di Lin, Ping Li, Wei Feng, and Song Wang. Misf: Multi-level interactive siamese filtering for high-fidelity image inpainting. In *Proceedings of the IEEE/CVF Conference on Computer Vision and Pattern Recognition*, pages 1869–1878, 2022.
- [25] Guilin Liu, Fitsum A Reda, Kevin J Shih, Ting-Chun Wang, Andrew Tao, and Bryan Catanzaro. Image inpainting for irregular holes using partial convolutions. In *European Conference on Computer Vision (ECCV)*, pages 85–100, 2018.
- [26] Zhihao Liu, Hui Yin, Yang Mi, Mengyang Pu, and Song Wang. Shadow removal by a lightness-guided network with training

- on unpaired data. *IEEE Transactions on Image Processing*, 30:1853–1865, 2021.
- [27] Zhihao Liu, Hui Yin, Xinyi Wu, Zhenyao Wu, Yang Mi, and Song Wang. From shadow generation to shadow removal. In *Proceedings of the IEEE/CVF Conference on Computer Vision and Pattern Recognition*, pages 4927–4936, 2021.
 - [28] Li-Qian Ma, Jue Wang, Eli Shechtman, Kalyan Sunkavalli, and Shi-Min Hu. Appearance harmonization for single image shadow removal. In *Computer Graphics Forum*, volume 35, pages 189–197. Wiley Online Library, 2016.
 - [29] Ben Mildenhall, Jonathan T Barron, Jiawen Chen, Dillon Sharlet, Ren Ng, and Robert Carroll. Burst denoising with kernel prediction networks. In *Proceedings of the IEEE conference on computer vision and pattern recognition*, pages 2502–2510, 2018.
 - [30] Sohail Nadimi and Bir Bhanu. Physical models for moving shadow and object detection in video. *IEEE transactions on pattern analysis and machine intelligence*, 26(8):1079–1087, 2004.
 - [31] Kamyar Nazeri, Eric Ng, Tony Joseph, Faisal Qureshi, and Mehran Ebrahimi. Edgeconnect: Structure guided image inpainting using edge prediction. In *IEEE/CVF International Conference on Computer Vision (ICCV) Workshops*, Oct 2019.
 - [32] Liangqiong Qu, Jiandong Tian, Shengfeng He, Yandong Tang, and Rynson WH Lau. Deshadownet: A multi-context embedding deep network for shadow removal. In *Proceedings of the IEEE Conference on Computer Vision and Pattern Recognition*, pages 4067–4075, 2017.
 - [33] Andres Sanin, Conrad Sanderson, and Brian C Lovell. Improved shadow removal for robust person tracking in surveillance scenarios. In *ICPR*, pages 141–144, 2010.
 - [34] Jin Wan, Hui Yin, Zhenyao Wu, Xinyi Wu, Yanting Liu, and Song Wang. Style-guided shadow removal. In *Proceedings of the European Conference on Computer Vision (ECCV)*, 2022.
 - [35] Chunxia Xiao, Ruiyun She, Donglin Xiao, and Kwan-Liu Ma. Fast shadow removal using adaptive multi-scale illumination transfer. In *Computer Graphics Forum*, volume 32, pages 207–218. Wiley Online Library, 2013.
 - [36] Zhenda Xie, Zheng Zhang, Yue Cao, Yutong Lin, Jianmin Bao, Zhuliang Yao, Qi Dai, and Han Hu. Simmim: A simple framework for masked image modeling. In *Proceedings of the IEEE/CVF Conference on Computer Vision and Pattern Recognition*, pages 9653–9663, 2022.
 - [37] Qingxiong Yang, Kar-Han Tan, and Narendra Ahuja. Shadow removal using bilateral filtering. *IEEE Transactions on Image processing*, 21(10):4361–4368, 2012.
 - [38] Liming Zhai, Felix Juefei-Xu, Qing Guo, Xiaofei Xie, Lei Ma, Wei Feng, Shengchao Qin, and Yang Liu. It’s raining cats or dogs? adversarial rain attack on dnn perception. *arXiv preprint arXiv:2009.09205*, 2020.
 - [39] Richard Zhang, Phillip Isola, Alexei A Efros, Eli Shechtman, and Oliver Wang. The unreasonable effectiveness of deep features as a perceptual metric. In *IEEE/CVF Conference on Computer Vision and Pattern Recognition (CVPR)*, pages 586–595, 2018.
 - [40] Wuming Zhang, Xi Zhao, Jean-Marie Morvan, and Liming Chen. Improving shadow suppression for illumination robust face recognition. *IEEE transactions on pattern analysis and machine intelligence*, 41(3):611–624, 2018.
 - [41] Bolei Zhou, Agata Lapedriza, Aditya Khosla, Aude Oliva, and Antonio Torralba. Places: A 10 million image database for scene recognition. *IEEE Transactions on Pattern Analysis and Machine Intelligence*, 40(6):1452–1464, 2017.
 - [42] Jun-Yan Zhu, Taesung Park, Phillip Isola, and Alexei A Efros. Unpaired image-to-image translation using cycle-consistent adversarial networks. In *Proceedings of the IEEE international conference on computer vision*, pages 2223–2232, 2017.
 - [43] Yurui Zhu, Jie Huang, Xueyang Fu, Feng Zhao, Qibin Sun, and Zheng-Jun Zha. Bijective mapping network for shadow removal. In *Proceedings of the IEEE/CVF Conference on Computer Vision and Pattern Recognition*, pages 5627–5636, 2022.

Supplementary Material

In this material, we add the detailed architectures of the encoder-decoder mentioned in Sec.3.1 and the network of our method mentioned in Sec.4.2. Besides, we also add a detailed description of the loss functions mentioned in Sec.3.1 and Sec.3.2. To prove the advantage of our methods, we also provide some visualized comparison on the image level as well as the L_1 difference between the restored result and the corresponding ground truth on the A&B channels of LAB color space.

A. Network architecture

Training Network for Image Inpainting (Sec.3.1). Instead of using advanced inpainting networks (*e.g.*, MISF [24]), we employ a naive encoder-decoder network during the training for image inpainting. The detailed architecture of the encoder-decoder is shown in Table D.

The Network of Shadow-informed Dynamic Filtering (Sec.4.2). Our Shadow-informed Dynamic Filtering network consists of an Image Inpainting Branch and a Shadow Representation Branch. Both of Image Inpainting Branch and Shadow Representation Branch employ the same encoder-decoder network as shown in Table E. We perform dynamic filtering on the image level $\tilde{\mathbf{F}}_7$ and the feature level $\tilde{\mathbf{F}}_3$.

B. Loss Functions

Training Network for Image Inpainting (Sec.3.1). Given a corrupted image \mathbf{I} where the corrupted regions are indicated by a binary mask \mathbf{M} as well as the corresponding ground truth \mathbf{I}^* and restored result $\hat{\mathbf{I}}$ by generator \mathcal{G} . We follow [24] and [31] employ ℓ_1 loss, GAN loss, Perceptual loss, and Style loss during the training. Specifically, the ℓ_1 loss is defined as:

$$\mathcal{L}_{\ell_1} = \frac{1}{\text{Mean}(\mathbf{M})} \|\hat{\mathbf{I}} - \mathbf{I}^*\|_1. \quad (6)$$

The objective functions to optimize the generator \mathcal{G} and discriminator \mathcal{D} are defined as:

$$\mathcal{L}_{Gen}(\mathcal{G}) = \mathbb{E}_{\mathbf{I} \sim p(\mathbf{I})} \log[1 - \mathcal{D}(\mathcal{G}(\mathbf{I}))], \quad (7)$$

$$\mathcal{L}_{Dis}(\mathcal{D}) = \frac{1}{2} \mathbb{E}_{\mathbf{I} \sim p(\mathbf{I})} \log[\mathcal{D}(\mathcal{G}(\mathbf{I}))] + \frac{1}{2} \mathbb{E}_{\mathbf{I}^* \sim p(\mathbf{I}^*)} \log[1 - \mathcal{D}(\mathbf{I}^*)]. \quad (8)$$

The GAN loss is defined as:

$$\mathcal{L}_{GAN} = \mathcal{L}_{Gen}(\mathcal{G}) + \mathcal{L}_{Dis}(\mathcal{D}). \quad (9)$$

To calculate the Perceptual loss, we use the VGG-19 pretrained network ω to extract the feature from \mathbf{I}^* and

$\hat{\mathbf{I}}$. ω_i denote the feature comes from each layer of *relu1_1, relu2_1, relu3_1, relu4_1, relu5_1* respectively. The Perceptual loss is defined as:

$$\mathcal{L}_{Perc} = \mathbb{E} \left[\sum_{i=1} \frac{1}{N_i} \|\omega_i(\mathbf{I}^*) - \omega_i(\hat{\mathbf{I}})\|_1 \right], \quad (10)$$

where we set N_i to 1. The same features are used to calculate the Style loss which is shown as:

$$\mathcal{L}_{Style} = \mathbb{E} \left[\|\mathbf{G}(\omega_i(\mathbf{I}^* * \mathbf{M})) - \mathbf{G}(\omega_i(\hat{\mathbf{I}} * \mathbf{M}))\|_1 \right], \quad (11)$$

where \mathbf{G} is a Gram matrix constructed from the feature ω_i . Then, the total loss function is defined as:

$$\mathcal{L}(\hat{\mathbf{I}}, \mathbf{I}^*) = \lambda_1 \mathcal{L}_{\ell_1} + \lambda_2 \mathcal{L}_{GAN} + \lambda_3 \mathcal{L}_{Perc} + \lambda_4 \mathcal{L}_{Style}, \quad (12)$$

where we set $\lambda_1 = 1$, $\lambda_2 = 0.1$, $\lambda_3 = 0.1$, and $\lambda_4 = 250$.

Training Network for Shadow Removal (Sec.3.2). Given a shadow image \mathbf{I} where the shadow regions are indicated by a binary mask \mathbf{M} as well as the corresponding ground truth shadow-free image \mathbf{I}^* and restored result $\hat{\mathbf{I}}$. During the training, we only use ℓ_1 loss which is shown as:

$$\mathcal{L}_{\ell_1} = \frac{\lambda_1}{\text{Mean}(\mathbf{M})} \|\hat{\mathbf{I}} - \mathbf{I}^*\|_1, \quad (13)$$

where we set $\lambda_1 = 1$.

C. Visualization Comparison

To prove the effectiveness of our method. We have provided the visualized comparison on the image level (see the first and third rows) as well as the L_1 difference between the restored result and the corresponding ground truth on A&B channels of LAB color space (see the second and fourth rows) as shown in Fig. A and Fig. B. The visualized L_1 difference is the averaged results coming from the difference between channels A&B and their corresponding ground truth. The samples in Fig. A and Fig. B are come from ISTD+ dataset [21] and SRD dataset [32] respectively. From the visualization comparison, we can find that ① With our method the shadow boundary in the restored result is more smooth even indistinguishable by human eyes. ② On the LAB color space, the color difference between the restored result and the corresponding ground truth is smaller by using our method.

	Input size of each layer	Conv. layers
Encoder	256 × 256 256 × 256 128 × 128	Conv(4, 64, 7, 1, 3) Conv(64, 128, 4, 2, 1) Conv(128, 256, 4, 2, 1)
Resnet Block × 8	64 × 64 64 × 64	Conv(256, 256, 3, 1, 1) Conv(256, 256, 3, 1, 1)
Decoder	64 × 64 128 × 128 256 × 256	ConvTran(256, 128, 4, 2, 1) ConvTran(128, 64, 4, 2, 1) ConvTran(64, 3, 7, 1, 3)

Table D. Detailed architecture of naive encoder-decoder. The input size of each layer is defined as $H \times W$. The parameters of 'Conv&ConvTran' are the numbers of input and output channels, kernel size, stride, and padding respectively.

Table E. Detailed architecture of our method. The input size of each layer is defined as $H \times W$. The parameters of 'Conv&ConvTran' are the numbers of input and output channels, kernel size, stride, and padding respectively.

	Image Inpainting Branch ($\phi^{-1}(\phi(\cdot))$)				Shadow Representation Branch ($\psi(\cdot)$)			
	In.	Out.	Out. size	Conv. layers	In.	Out.	Out. size	Conv. layers
Encoder	$\tilde{\mathbf{I}}$ $\tilde{\mathbf{F}}_1$ $\tilde{\mathbf{F}}_2$	$\tilde{\mathbf{F}}_1$ $\tilde{\mathbf{F}}_2$ $\tilde{\mathbf{F}}_3$	256 × 256 128 × 128 64 × 64	Conv(4, 64, 7, 1, 3) Conv(64, 128, 4, 2, 1) Conv(128, 256, 4, 2, 1)	\mathbf{I} \mathbf{F}_1 \mathbf{F}_2	\mathbf{F}_1 \mathbf{F}_2 \mathbf{F}_3	256 × 256 128 × 128 64 × 64	Conv(4, 64, 7, 1, 3) Conv(64, 128, 4, 2, 1) Conv(128, 256, 4, 2, 1)
Dynamic Filtering	$[\tilde{\mathbf{F}}_3 \otimes \mathbf{K}_3, \mathbf{R}_3]$	$\tilde{\mathbf{F}}'_3$	64 × 64	Conv ³ _{fusion} (512, 256, 3, 1, 1)	\mathbf{F}_3 \mathbf{F}_3	\mathbf{K}_3 \mathbf{R}_3	64 × 64 64 × 64	Conv ³ _{kernel} (256, 256 × 3 ² , 1, 1, 0) Conv ³ _{offset} (256, 256, 3, 1, 1)
Resnet Block × 8	$\tilde{\mathbf{F}}'_3$ $\tilde{\mathbf{F}}_4$	$\tilde{\mathbf{F}}_4$ $\tilde{\mathbf{F}}_4$	64 × 64 64 × 64	Conv(256, 256, 3, 1, 1) Conv(256, 256, 3, 1, 1)	\mathbf{F}_3 \mathbf{F}_4	\mathbf{F}_4 \mathbf{F}_4	64 × 64 64 × 64	Conv(256, 256, 3, 1, 1) Conv(256, 256, 3, 1, 1)
Decoder	$\tilde{\mathbf{F}}_4$ $\tilde{\mathbf{F}}_5$ $\tilde{\mathbf{F}}_6$	$\tilde{\mathbf{F}}_5$ $\tilde{\mathbf{F}}_6$ $\tilde{\mathbf{F}}_7$	64 × 64 128 × 128 256 × 256	ConvTran(256, 128, 4, 2, 1) ConvTran(128, 64, 4, 2, 1) ConvTran(64, 3, 7, 1, 3)	\mathbf{F}_4 \mathbf{F}_5 \mathbf{F}_6	\mathbf{F}_5 \mathbf{F}_6 \mathbf{F}_7	64 × 64 128 × 128 256 × 256	ConvTran(256, 128, 4, 2, 1) ConvTran(128, 64, 4, 2, 1) ConvTran(64, 64, 3, 1, 1)
Dynamic Filtering	$[\tilde{\mathbf{F}}_7 \otimes \mathbf{K}_7, \mathbf{R}_7]$	$\hat{\mathbf{I}}$	256 × 256	Conv ⁷ _{fusion} (6, 3, 3, 1, 1)	\mathbf{F}_7 \mathbf{F}_7	\mathbf{K}_7 \mathbf{R}_7	256 × 256 256 × 256	Conv ⁷ _{kernel} (64, 3 × 3 ² , 1, 1, 0) Conv ⁷ _{offset} (64, 3, 7, 1, 3)

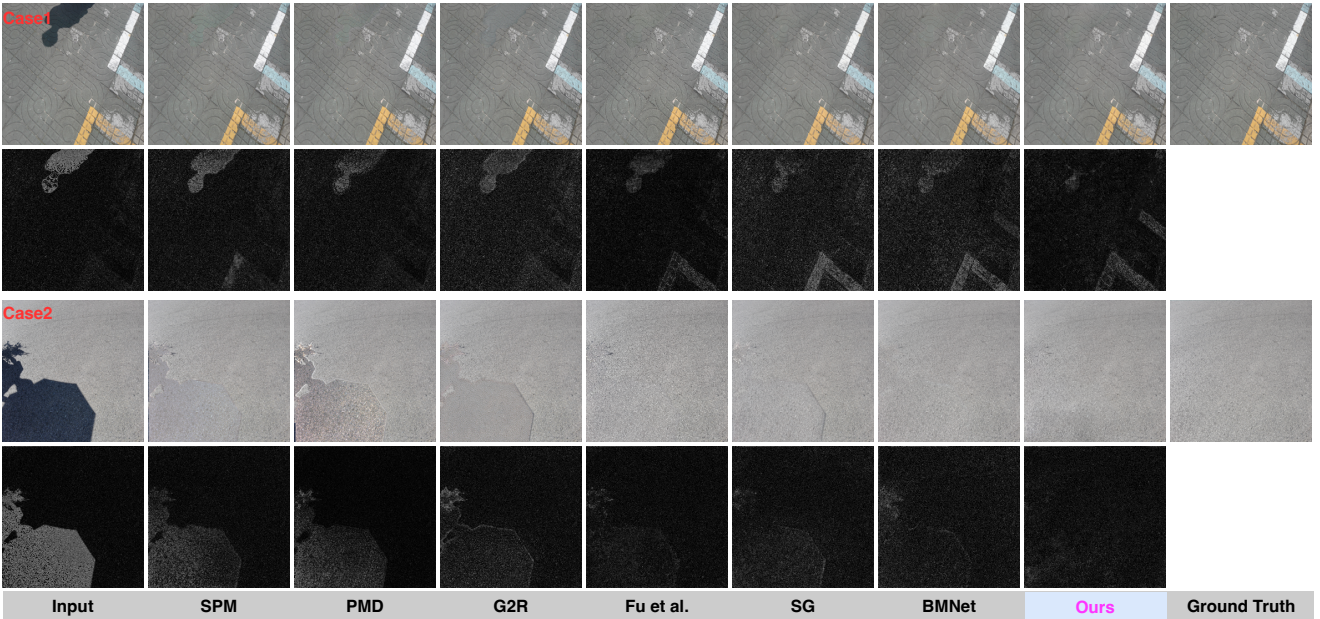


Figure A. Comparison on ISTD+ dataset [21]. From left to right are input shadow image, SPM [21], PMD [22], G2R [27], Fu et al. [8], SG [34], BMNet [43], Our method, and corresponding ground truth respectively.

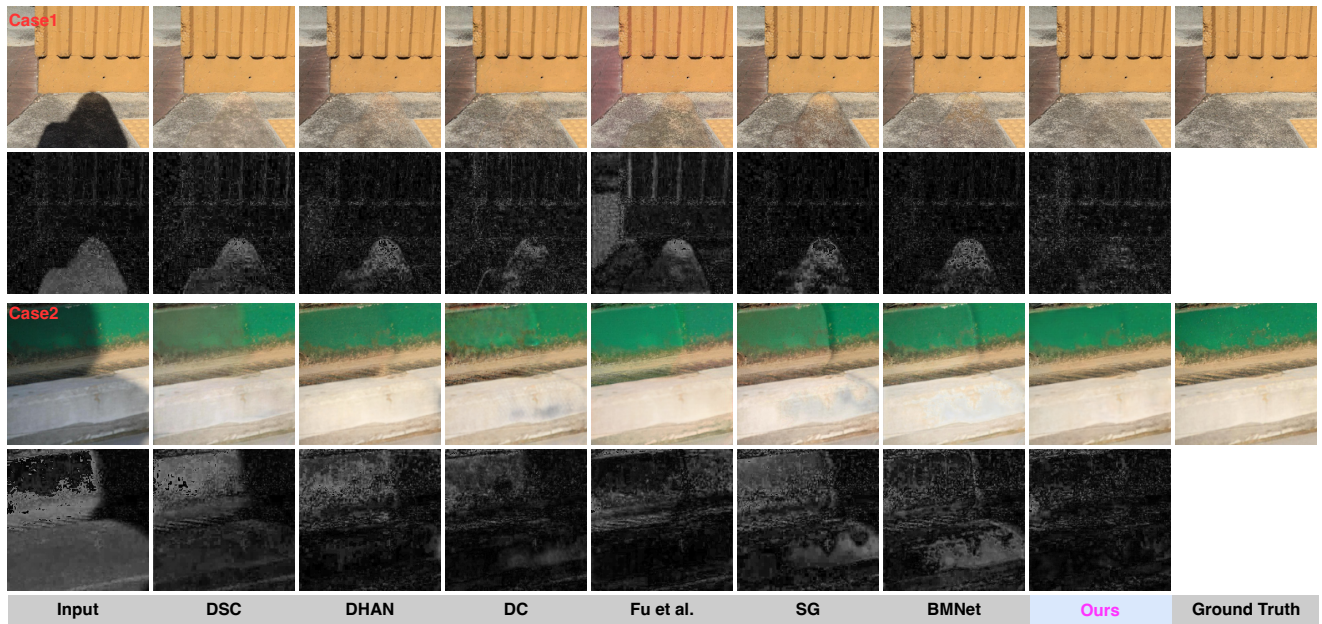


Figure B. Comparison on SRD dataset [32]. From left to right are input shadow image, DSC [17], DHAN [4], DC [19], Fu et al. [8], SG [34], BMNet [43], Our method, and the corresponding ground truth respectively.